

Determination of eddy currents in the vacuum vessel of spherical tokamaks

G.O. Ludwig *, E. Del Bosco, J.G. Ferreira, L.A. Berni

*Associated Plasma Laboratory, National Space Research Institute
12227-010, São José dos Campos, SP, Brazil*

1 Introduction

The distribution of currents induced in the vacuum vessel of spherical tokamaks is required for startup simulations, equilibrium reconstruction and control. To take into account the effect of these eddy currents, the vacuum vessel is usually modeled as a large collection of conducting rings [1, 2, 3]. Then, given the measured electromotive force (emf) obtained from a toroidal loop placed near each ring, the current flowing in the ring is calculated dividing the emf by the ring resistance. This model assumes that the current in each ring is uniform, requiring the division of the vacuum vessel wall in a large number of segments, for adequate representation, and the interpolation of the signals obtained from a finite number of measuring loops. In this way, the coupling between diverse regions of the vacuum vessel and external sources is not properly taken into account and the method fails at fast time scales. Recently [4, 5], a new method has been developed that accurately describes the local and non-local fast effects of different regions of the vessel. The method solves the integro-differential equation that governs the evolution of the surface current density induced in a thin axisymmetric shell, reducing the problem to a circuit model. In this paper, the model presented in [5] is improved dividing the vacuum vessel of ETE in three sectors of different thicknesses, according with the actual fabrication. This allows a better representation of the jumps in the surface current density for a continuous emf across the discontinuous wall resistance. Besides, the new formulation provides a link with the usual conducting rings model. The emf calculated with the new model is compared with the voltage measured in loop voltage sensors placed along the poloidal perimeter of the vacuum vessel of ETE. Also, the improved calculations are compared with previously presented measurements of the current distribution on the vacuum vessel wall [4, 5].

2 Formulation of the problem

The toroidal surface current density in a thin axisymmetric shell is related to the poloidal flux function by Faraday's law [5]

$$K_T(\theta, t) = -\frac{\sigma_s \delta_s}{2\pi h_\zeta(\theta)} \frac{\partial \Phi_P(\theta, t)}{\partial t}, \quad (1)$$

where σ_s and δ_s are the local values of the shell conductivity and thickness, respectively. The centerline of the vacuum vessel wall is modeled by a spectral representation in local curvilinear coordinates specified by the scale factors $h_\zeta(\theta)$ and $h_\theta(\theta)$. In terms of the Green's function $G(\theta, \theta')$ for the axisymmetric Ampère's law the evolution of eddy currents in the shell is governed by the integro-differential equation

$$\frac{2\pi h_\zeta(\theta)}{\sigma_s \delta_s} K_T(\theta, t) = -\mu_0 \int_0^{2\pi} \frac{\partial K_T(\theta')}{\partial t} G(\theta, \theta') h_\theta(\theta') d\theta' - \frac{\partial \Phi_{P,ext}(\theta, t)}{\partial t}, \quad (2)$$

where $\Phi_{P,ext}(\theta, t)$ is the poloidal flux function produced on the vessel wall by the external sources only, and the total toroidal current induced in the shell is

$$I_T(t) = \int_0^{2\pi} K_T(\theta, t) h_\theta(\theta) d\theta. \quad (3)$$

*Corresponding author. *E-mail address:* ludwig@plasma.inpe.br

Now, the vacuum vessel wall of ETE is formed by three shells of different thicknesses, joined at the poloidal angles $\theta_1 = 0.3997$ (22.90°), $\theta_2 = 2.1326$ (122.19°) and their conjugate angles in the spectral representation. The thicknesses of the external cylindrical wall, the torispherical head wall and the internal cylindrical wall are $\delta_1 = 4.80$ mm, $\delta_2 = 6.35$ mm and $\delta_3 = 1.20$ mm, respectively. On the six sectors defined by θ_1 and θ_2 along the vessel centerline, the surface current density has the following Fourier series representations:

$$\begin{aligned}
0 < \theta < \theta_1 : K_T^{(1)}(\theta, t) &= \frac{1}{2\pi h_\theta(\theta)} \sum_{n=0}^{\infty} I_n^{(1)}(t) \cos \frac{n\pi\theta}{\theta_1}, \\
\theta_1 < \theta < \theta_2 : K_T^{(2)}(\theta, t) &= \frac{1}{2\pi h_\theta(\theta)} \sum_{n=0}^{\infty} I_n^{(2)}(t) \cos \frac{n\pi(\theta - \theta_1)}{\theta_2 - \theta_1}, \\
\theta_2 < \theta < \pi : K_T^{(3)}(\theta, t) &= \frac{1}{2\pi h_\theta(\theta)} \sum_{n=0}^{\infty} I_n^{(3)}(t) \cos \frac{n\pi(\theta - \theta_2)}{\pi - \theta_2}, \\
\pi < \theta < 2\pi - \theta_2 : K_T^{(4)}(\theta, t) &= K_T^{(3)}(2\pi - \theta, t), \\
2\pi - \theta_2 < \theta < 2\pi - \theta_1 : K_T^{(5)}(\theta, t) &= K_T^{(2)}(2\pi - \theta, t), \\
2\pi - \theta_1 < \theta < 2\pi : K_T^{(6)}(\theta, t) &= K_T^{(1)}(2\pi - \theta, t).
\end{aligned} \tag{4}$$

The total current in the vacuum vessel wall becomes

$$I_T(t) = \frac{\theta_1}{\pi} I_0^{(1)}(t) + \frac{\theta_2 - \theta_1}{\pi} I_0^{(2)}(t) + \frac{\pi - \theta_2}{\pi} I_0^{(3)}(t). \tag{5}$$

For continuous electromotive force the surface current density must satisfy the jump conditions

$$\begin{aligned}
\frac{K_T^{(1)}(\theta_1, t)}{\sigma_1 \delta_1} &= \frac{K_T^{(2)}(\theta_1, t)}{\sigma_2 \delta_2}, \\
\frac{K_T^{(2)}(\theta_2, t)}{\sigma_2 \delta_2} &= \frac{K_T^{(3)}(\theta_2, t)}{\sigma_3 \delta_3},
\end{aligned} \tag{6}$$

which can be used to verify the accuracy of the solution. In principle, these conditions can be used to eliminate any two Fourier components, reducing the number of circuit differential equations that must be solved for them. However, imposing these conditions enhances the high order harmonics and introduces spurious oscillations in the surface current density profile along the vacuum vessel wall, although with a negligible effect on the loop voltage calculated from all the flux sources. In this paper the calculations are performed without imposing the jump conditions.

Substituting the Fourier expansions in the integro-differential equation that governs the surface current density evolution, multiplying the resulting equations by $\pi^{-1} \cos(m\pi\theta/\theta_1)$, $\pi^{-1} \cos[m\pi(\theta - \theta_1)/(\theta_2 - \theta_1)]$ and $\pi^{-1} \cos[m\pi(\theta - \theta_2)/(\pi - \theta_2)]$ according to the range of validity in the poloidal angle θ , and integrating over the range of validity, one obtains a truncated set of $3(\ell + 1)$ circuit equations for the Fourier coefficients $I_n^{(1)}(t)$, $I_n^{(2)}(t)$ and $I_n^{(3)}(t)$ taking $m = 0, 1, 2 \dots \ell$ and $n = 0, 1, 2 \dots \ell$

$$\begin{aligned}
&\sum_{n=0}^{\ell} \left(R_{mn}^{(1)} I_n^{(1)}(t) + L_{mn}^{(1)} \frac{dI_n^{(1)}(t)}{dt} + M_{mn}^{(1,2)} \frac{dI_n^{(2)}(t)}{dt} + M_{mn}^{(1,3)} \frac{dI_n^{(3)}(t)}{dt} \right) \\
&= -\frac{d}{dt} \left(\frac{1}{\pi} \int_0^{\theta_1} \Phi_{P,ext}(\theta, t) \cos \frac{m\pi\theta}{\theta_1} d\theta \right), \\
&\sum_{n=0}^{\ell} \left(R_{mn}^{(2)} I_n^{(2)}(t) + L_{mn}^{(2)} \frac{dI_n^{(2)}(t)}{dt} + M_{mn}^{(2,1)} \frac{dI_n^{(1)}(t)}{dt} + M_{mn}^{(2,3)} \frac{dI_n^{(3)}(t)}{dt} \right) \\
&= -\frac{d}{dt} \left(\frac{1}{\pi} \int_{\theta_1}^{\theta_2} \Phi_{P,ext}(\theta, t) \cos \frac{m\pi(\theta - \theta_1)}{\theta_2 - \theta_1} d\theta \right), \\
&\sum_{n=0}^{\ell} \left(R_{mn}^{(3)} I_n^{(3)}(t) + L_{mn}^{(3)} \frac{dI_n^{(3)}(t)}{dt} + M_{mn}^{(3,1)} \frac{dI_n^{(1)}(t)}{dt} + M_{mn}^{(3,2)} \frac{dI_n^{(2)}(t)}{dt} \right) \\
&= -\frac{d}{dt} \left(\frac{1}{\pi} \int_{\theta_2}^{\pi} \Phi_{P,ext}(\theta, t) \cos \frac{m\pi(\theta - \theta_2)}{\pi - \theta_2} d\theta \right).
\end{aligned} \tag{7}$$

The resistance coefficients in these equations are defined by

$$\begin{aligned}
R_{mn}^{(1)} &= \frac{1}{\pi\sigma_1\delta_1} \int_0^{\theta_1} \frac{h_\zeta(\theta)}{h_\theta(\theta)} \cos \frac{m\pi\theta}{\theta_1} \cos \frac{n\pi\theta}{\theta_1} d\theta, \\
R_{mn}^{(2)} &= \frac{1}{\pi\sigma_2\delta_2} \int_{\theta_1}^{\theta_2} \frac{h_\zeta(\theta)}{h_\theta(\theta)} \cos \frac{m\pi(\theta-\theta_1)}{\theta_2-\theta_1} \cos \frac{n\pi(\theta-\theta_1)}{\theta_2-\theta_1} d\theta, \\
R_{mn}^{(3)} &= \frac{1}{\pi\sigma_3\delta_3} \int_{\theta_2}^{\pi} \frac{h_\zeta(\theta)}{h_\theta(\theta)} \cos \frac{m\pi(\theta-\theta_2)}{\pi-\theta_2} \cos \frac{n\pi(\theta-\theta_2)}{\pi-\theta_2} d\theta,
\end{aligned} \tag{8}$$

the self-inductance coefficients by

$$\begin{aligned}
L_{mn}^{(1)} &= \frac{\mu_0}{2\pi^2} \int_0^{\theta_1} \left[\left(\int_0^{\theta-\epsilon} + \int_{\theta+\epsilon}^{\theta_1} \right) G(\theta, \theta') + \int_0^{\theta_1} G(\theta, -\theta') \right] \cos \frac{m\pi\theta}{\theta_1} \cos \frac{n\pi\theta'}{\theta_1} d\theta' d\theta \\
&\quad + \frac{\mu_0\epsilon}{\pi^2} \int_0^{\theta_1} h_\zeta(\theta) \left[\ln \left(\frac{8h_\zeta(\theta)}{\epsilon h_\theta(\theta)} \right) - 1 \right] \cos \frac{m\pi\theta}{\theta_1} \cos \frac{n\pi\theta}{\theta_1} d\theta, \\
L_{mn}^{(2)} &= \frac{\mu_0}{2\pi^2} \int_{\theta_1}^{\theta_2} \left[\left(\int_{\theta_1}^{\theta-\epsilon} + \int_{\theta+\epsilon}^{\theta_2} \right) G(\theta, \theta') + \int_{\theta_1}^{\theta_2} G(\theta, -\theta') \right] \cos \frac{m\pi(\theta-\theta_1)}{\theta_2-\theta_1} \cos \frac{n\pi(\theta'-\theta_1)}{\theta_2-\theta_1} d\theta' d\theta \\
&\quad + \frac{\mu_0\epsilon}{\pi^2} \int_{\theta_1}^{\theta_2} h_\zeta(\theta) \left[\ln \left(\frac{8h_\zeta(\theta)}{\epsilon h_\theta(\theta)} \right) - 1 \right] \cos \frac{m\pi(\theta-\theta_1)}{\theta_2-\theta_1} \cos \frac{n\pi(\theta-\theta_1)}{\theta_2-\theta_1} d\theta, \\
L_{mn}^{(3)} &= \frac{\mu_0}{2\pi^2} \int_{\theta_2}^{\pi} \left[\left(\int_{\theta_2}^{\theta-\epsilon} + \int_{\theta+\epsilon}^{\pi} \right) G(\theta, \theta') + \int_{\theta_2}^{\pi} G(\theta, -\theta') \right] \cos \frac{m\pi(\theta-\theta_2)}{\pi-\theta_2} \cos \frac{n\pi(\theta'-\theta_2)}{\pi-\theta_2} d\theta' d\theta \\
&\quad + \frac{\mu_0\epsilon}{\pi^2} \int_{\theta_2}^{\pi} h_\zeta(\theta) \left[\ln \left(\frac{8h_\zeta(\theta)}{\epsilon h_\theta(\theta)} \right) - 1 \right] \cos \frac{m\pi(\theta-\theta_2)}{\pi-\theta_2} \cos \frac{n\pi(\theta-\theta_2)}{\pi-\theta_2} d\theta,
\end{aligned} \tag{9}$$

and the mutual inductance coefficients by

$$\begin{aligned}
M_{mn}^{(1,2)} &= \frac{\mu_0}{2\pi^2} \int_0^{\theta_1} \int_{\theta_1}^{\theta_2} [G(\theta, \theta') + G(\theta, -\theta')] \cos \frac{m\pi\theta}{\theta_1} \cos \frac{n\pi(\theta'-\theta_1)}{\theta_2-\theta_1} d\theta' d\theta, \\
M_{mn}^{(1,3)} &= \frac{\mu_0}{2\pi^2} \int_0^{\theta_1} \int_{\theta_2}^{\pi} [G(\theta, \theta') + G(\theta, -\theta')] \cos \frac{m\pi\theta}{\theta_1} \cos \frac{n\pi(\theta'-\theta_2)}{\pi-\theta_2} d\theta' d\theta, \\
M_{mn}^{(2,1)} &= \frac{\mu_0}{2\pi^2} \int_{\theta_1}^{\theta_2} \int_0^{\theta_1} [G(\theta, \theta') + G(\theta, -\theta')] \cos \frac{m\pi(\theta-\theta_1)}{\theta_2-\theta_1} \cos \frac{n\pi\theta'}{\theta_1} d\theta' d\theta, \\
M_{mn}^{(2,3)} &= \frac{\mu_0}{2\pi^2} \int_{\theta_1}^{\theta_2} \int_{\theta_2}^{\pi} [G(\theta, \theta') + G(\theta, -\theta')] \cos \frac{m\pi(\theta-\theta_1)}{\theta_2-\theta_1} \cos \frac{n\pi(\theta'-\theta_2)}{\pi-\theta_2} d\theta' d\theta, \\
M_{mn}^{(3,1)} &= \frac{\mu_0}{2\pi^2} \int_{\theta_2}^{\pi} \int_0^{\theta_1} [G(\theta, \theta') + G(\theta, -\theta')] \cos \frac{m\pi(\theta-\theta_2)}{\pi-\theta_2} \cos \frac{n\pi\theta'}{\theta_1} d\theta' d\theta, \\
M_{mn}^{(3,2)} &= \frac{\mu_0}{2\pi^2} \int_{\theta_2}^{\pi} \int_{\theta_1}^{\theta_2} [G(\theta, \theta') + G(\theta, -\theta')] \cos \frac{m\pi(\theta-\theta_2)}{\pi-\theta_2} \cos \frac{n\pi(\theta'-\theta_1)}{\theta_2-\theta_1} d\theta' d\theta.
\end{aligned} \tag{10}$$

The small angle $\epsilon \ll 1$ is introduced in the expressions of the self-inductance coefficients to handle numerically the singularity in the Green's function. The resistance and inductance coefficients satisfy the following symmetry properties:

$$\begin{aligned}
R_{mn}^{(1)} &= R_{nm}^{(1)}, & R_{mn}^{(2)} &= R_{nm}^{(2)}, & R_{mn}^{(3)} &= R_{nm}^{(3)}, \\
L_{mn}^{(1)} &= L_{nm}^{(1)}, & L_{mn}^{(2)} &= L_{nm}^{(2)}, & L_{mn}^{(3)} &= L_{nm}^{(3)}, \\
M_{mn}^{(2,1)} &= M_{nm}^{(1,2)}, & M_{mn}^{(3,1)} &= M_{nm}^{(1,3)}, & M_{mn}^{(3,2)} &= M_{nm}^{(2,3)}.
\end{aligned} \tag{11}$$

The surface current density induced in the vacuum vessel wall can be determined by the circuit equations in two ways: dividing the wall in a small number of sectors with a relatively large number of Fourier coefficients representing the current in each sector, as indicated above, or dividing the wall in a large number of sectors with a small number of coefficients in each sector. In the latter case, taking $\ell = 0$ corresponds to dividing the wall in a large number of rings with uniform current density, similarly to the model adopted in previous works [1, 2, 3], though with a precise definition for the coefficients in the circuit model.

The right-hand side of the circuit equations can be written in terms of the currents circulating in the

external sources using the appropriate mutual inductance coefficients

$$\begin{aligned}
& -\frac{d}{dt} \left(\frac{1}{\pi} \int_0^{\theta_1} \Phi_{P,ext}(\theta, t) \cos \frac{m\pi\theta}{\theta_1} d\theta \right) \\
& = -M_{m,\Omega}^{(1)} \frac{dI_\Omega}{dt} - \sum_{n=1}^{\infty} M_{m,\Omega n}^{(1)} \frac{dI_n}{dt} - M_{m,TF}^{(1)} \frac{dI_{TF}(t)}{dt} - \sum_k M_{m,k}^{(1)} \frac{dI_k(t)}{dt}, \\
& -\frac{d}{dt} \left(\frac{1}{\pi} \int_{\theta_1}^{\theta_2} \Phi_{P,ext}(\theta, t) \cos \frac{m\pi(\theta - \theta_1)}{\theta_2 - \theta_1} d\theta \right) \\
& = -M_{m,\Omega}^{(2)} \frac{dI_\Omega}{dt} - \sum_{n=1}^{\infty} M_{m,\Omega n}^{(2)} \frac{dI_n}{dt} - M_{m,TF}^{(2)} \frac{dI_{TF}(t)}{dt} - \sum_k M_{m,k}^{(2)} \frac{dI_k(t)}{dt}, \\
& -\frac{d}{dt} \left(\frac{1}{\pi} \int_{\theta_2}^{\pi} \Phi_{P,ext}(\theta, t) \cos \frac{m\pi(\theta - \theta_2)}{\pi - \theta_2} d\theta \right) \\
& = -M_{m,\Omega}^{(3)} \frac{dI_\Omega}{dt} - \sum_{n=1}^{\infty} M_{m,\Omega n}^{(3)} \frac{dI_n}{dt} - M_{m,TF}^{(3)} \frac{dI_{TF}(t)}{dt} - \sum_k M_{m,k}^{(3)} \frac{dI_k(t)}{dt},
\end{aligned} \tag{12}$$

where $M_{m,\Omega}^{(s)}$, $M_{m,\Omega n}^{(s)}$, $M_{m,TF}^{(s)}$ and $M_{m,k}^{(s)}$ are the mutual inductances between the circuit for the Fourier component of order m of the surface current density in shell (s) and the ohmic heating (OH) system, the proximity effect current components in the OH system, the eddy currents in the central column of the toroidal field (TF) coil, and any additional external coils, respectively. The models for the currents induced in the central column of the TF coil and the proximity effect in the OH system are presented in detail in a forthcoming paper [6].

The corresponding voltage drop in the OH system is

$$\begin{aligned}
v_\Omega(t) & = R_\Omega I_\Omega(t) + L_\Omega \frac{dI_\Omega}{dt} + \sum_{n=1}^{\infty} L_n \frac{dI_n}{dt} + \frac{N_\Omega \ell_{eff}}{h_\Omega} \frac{d\Phi_{TF}}{dt} \\
& + \sum_{m=0}^{\ell} \left(M_{\Omega,m}^{(1)} \frac{dI_m^{(1)}(t)}{dt} + M_{\Omega,m}^{(2)} \frac{dI_m^{(2)}(t)}{dt} + M_{\Omega,m}^{(3)} \frac{dI_m^{(3)}(t)}{dt} \right) + \sum_k M_{\Omega,k} \frac{dI_k(t)}{dt},
\end{aligned} \tag{13}$$

where R_Ω and L_Ω are the resistance and inductance of the OH system, respectively, neglecting eddy current and proximity effects, L_n is the internal inductance associated with the proximity effect current components $I_n(t)$ in the OH system, $\Phi_{TF}(t)$ is the flux associated with eddy currents induced in the central column of the TF coil, $M_{\Omega,m}^{(s)} = M_{m,\Omega}^{(s)}$ are the mutual inductance coefficients between the components $I_m^{(s)}(t)$ of the surface current density in shell (s) and the OH system, and $M_{\Omega,k}$ is the mutual inductance coefficient between any additional external coils carrying the current $I_k(t)$ and the OH system. The parameters N_Ω and h_Ω refer to the number of turns and height of the OH solenoid, while ℓ_{eff} is the total length of the OH solenoid in series with the internal compensation coils, taking into account end effects.

3 Results

The model was applied to evaluate the currents induced in the vacuum vessel wall of the ETE spherical tokamak, using up to four harmonics ($\ell = 4$), and to calculate the loop voltage produced by the external sources and eddy currents, including vacuum vessel, central column and proximity effect components. Figure 1 shows the calculated (continuous lines) and experimental values (disks) of the currents in the OH system and vacuum vessel for a shot used to compare the loop voltage results. The locations of the loop voltage sensors around the poloidal perimeter of the ETE vessel are shown in Fig. 2. The comparison between the loop voltage measurements (disks) and calculations (continuous lines) is shown in Fig. 3. Pairs of loop voltage sensors placed symmetrically with respect to the equatorial plane produce practically identical signals represented by gray and black disks in Fig. 3. The agreement with theory and experiment is very good, with the largest discrepancy occurring at the position of sensor VS3. There, on the torispherical head, the inductance coefficients vary significantly with the radial distance and a large number of Fourier components is needed to describe correctly the jump in the surface current density at the outside corner. Furthermore, the sensor VS3 is not a perfectly axisymmetric toroidal loop, bending around the large ports on the torispherical head in a way not described by the model. Note that the signal on the axisymmetric internal loop voltage sensor VI, placed at a position almost symmetrical to VS3, just slightly farther from the vessel wall, shows a much better agreement with theory. Note also

that the sensors are placed close to the vessel wall, near the surface current source where the calculation is most difficult. Hence, the model should provide an excellent evaluation of the loop voltage in the region inside the vessel filled by the plasma. Now, at the initial peak of the loop voltage in the inner side of the vessel, the experimental points indicate a slightly faster time scale than the theoretical results. This is a consequence of the simplified model adopted for the proximity effect components. The geometry of the model does not take into account the presence, in the square conductor used in the OH system, of a large circular cooling hole, which leads to a complicated modal structure with faster time scales. Finally, the same kind of simplification in the geometry of the central column, without including the effects of insulation and cooling holes, seems to lead to a slight delay in the theoretical results, compared with the experimental results, on the longer time scale.

The improved model presented in this paper was also used to make comparisons with previously published results [5] of the eddy current distribution in sections of the ETE vacuum vessel wall. Again, Fig. 4 shows the currents in the OH system and the vacuum vessel for the current distribution test shot. Figure 5 shows the sections of the vacuum vessel wall used for measuring the eddy current distribution using a long, removable Rogowski coil. The comparison between experimental and theoretical results is shown in Fig. 6. The agreement is quite good, with the larger discrepancies occurring in the signals I2, I3 and I4, which correspond to the region on the torispherical head most difficult to be reproduced by the theory, as pointed out before. Moreover, the experimental results were obtained in subsequent shots, with a discrepancy of 8% in the total current. Indeed, signal I6 in Fig. 6 shows a peak value of 25 kA, which added to twice the peak value of 8 kA shown by signal I5 gives 41 kA that must be compared to the peak value of 38 kA in the total current in the vacuum vessel shown in Fig. 4. Now, comparing the results shown in Fig. 6 with the previously published ones [5], the new results present a much better agreement. This is partly because of the improvements introduced in the model, but the main difference arises from the approach taken regarding the equilibrium circuit. Although inactive (banks discharged), this circuit was present in the model used in reference [5], so that current could flow through the equilibrium coil as long as the voltage applied to it by the remaining poloidal circuits had the right polarity for driving the free-wheeling diode into conduction. However, it was later realized that the equilibrium coil had been temporarily disconnected for engineering tests during the same shots used for measuring the distribution of eddy currents and therefore its inclusion in the model was in fact inappropriate, a mistake which became the main reason for the time lag apparent in some signals of the previous publication.

Acknowledgment: This work was partially supported by the International Atomic Energy Agency under the Co-ordinated Research Project on Joint Research Using Small Tokamaks – Contract BRA/12932.

References

- [1] S.A. Sabbagh, S.M. Kaye, J. Menard, F. Paoletti, M. Bell, R.E. Bell, J.M. Bialek, M. Bitter, E.D. Fredrickson, D.A. Gates, A.H. Glasser, H. Kugel, L.L. Lao, B.P. LeBlanc, R. Maingi, R.J. Maqueda, E. Mazzucato, D. Mueller, M. Ono, S.F. Paul, M. Peng, C.H. Skinner, D. Stutman, G.A. Wurden, W. Zhu and NSTX Research Team 2001 Equilibrium properties of spherical torus plasmas in NSTX *Nucl. Fusion* **41** 1601-11
- [2] V.M. Amoskov, V.A. Belyakov, S.E. Bender, V.K. Gusev, A.A. Kavin, E.A. Lamzin, R.G. Levin, S.N. Sadakov, N.V. Sakharov, S.E. Sychevskii and O.G. Filatov 2003 Real-time determination of the position and shape of the plasma column from external magnetic measurements in the GLOBUS-M tokamak *Plasma Phys. Rep.* **29** 997-1008
- [3] D.A. Gates, J.E. Menard and R.J. Marsala 2004 Vessel eddy current measurement for the National Spherical Torus Experiment *Rev. Sci. Instrum.* **75** 5090-3
- [4] G.O. Ludwig, E. Del Bosco and J.G. Ferreira 2004 Modeling and measurement of eddy currents in the ETE spherical tokamak *Proc. 20th Int. Conf. on Fusion Energy 2004 (Vilamoura, 2004)*(Vienna: IAEA) CD-ROM file TH/P4-7 and <http://www-naweb.iaea.org/napc/physics/fec/fec2004/datasets/index.html>
- [5] G.O. Ludwig, E. Del Bosco and J.G. Ferreira 2005 Eddy currents in the vacuum vessel of the ETE spherical tokamak *Nucl. Fusion* **45** 675-684
- [6] G.O. Ludwig, J.G. Ferreira and E. Del Bosco 2005 Eddy currents in the central column of the ETE spherical tokamak *Fusion Eng. Design* In print

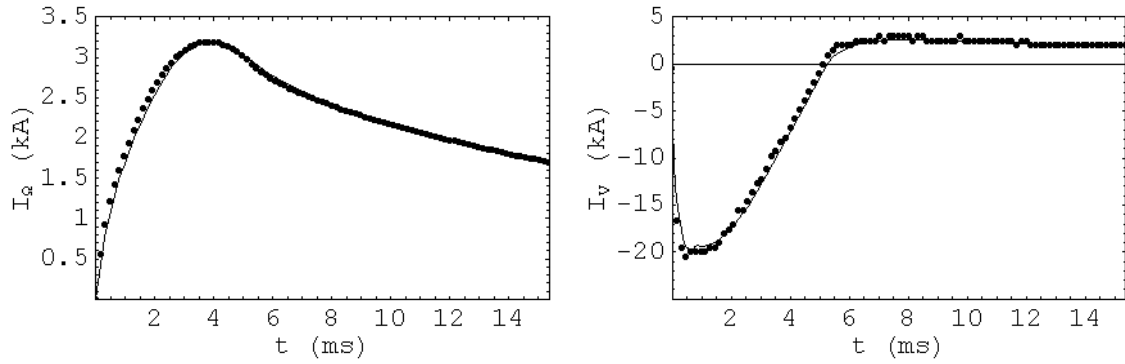


Figure 1: Current in the ohmic heating circuit (left) and total current induced in the vacuum vessel wall (right) for the loop voltage test shot. The continuous line and the disks correspond to calculated and measured values, respectively.

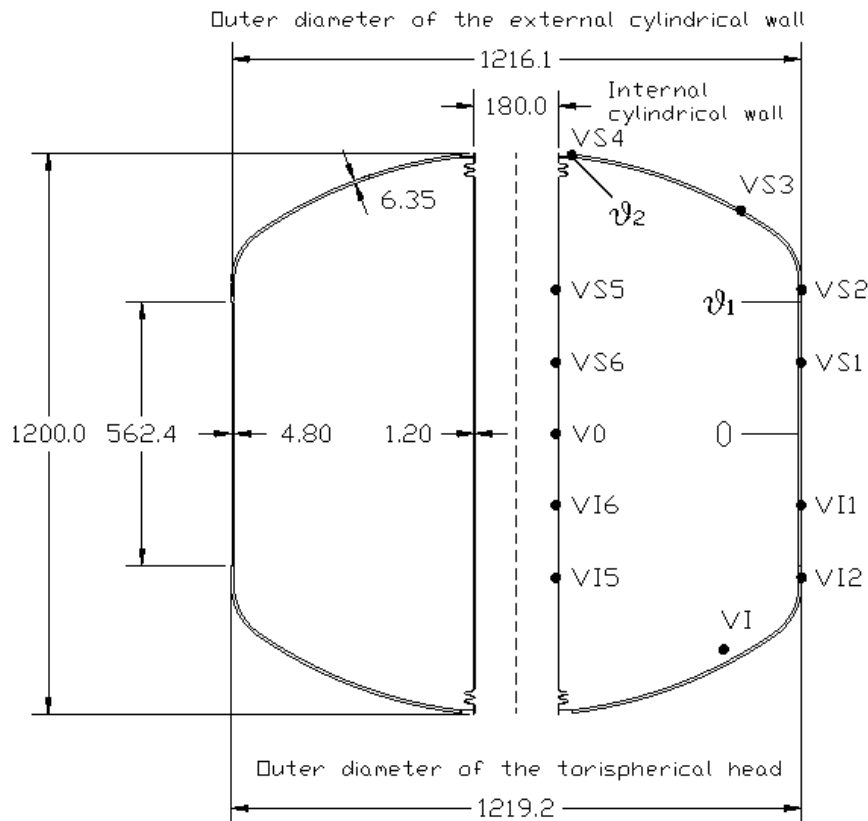


Figure 2: Cross-section of the ETE vacuum vessel showing the locations of the loop voltage sensors.

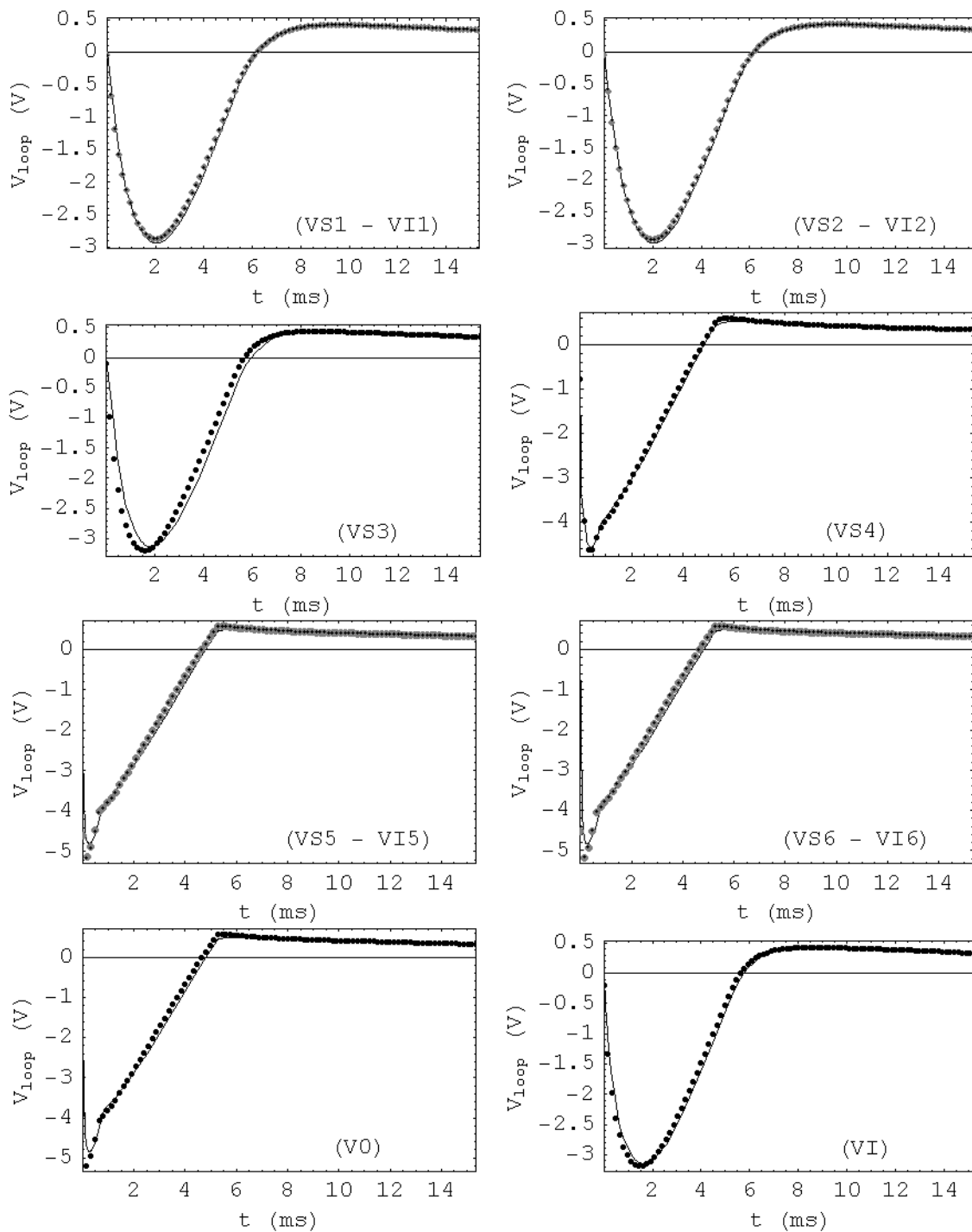


Figure 3: Comparison between the loop voltage measurements (disks) and the electromotive force calculated with the model (continuous lines).

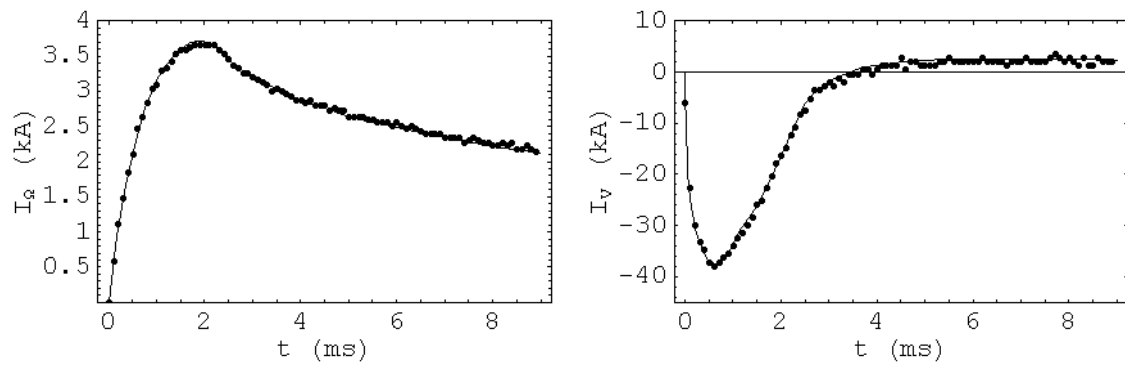


Figure 4: Current in the ohmic heating system (left) and total current induced in the vacuum vessel wall (right) for the current distribution test shot. The continuous line and the disks correspond to calculated and measured values, respectively.

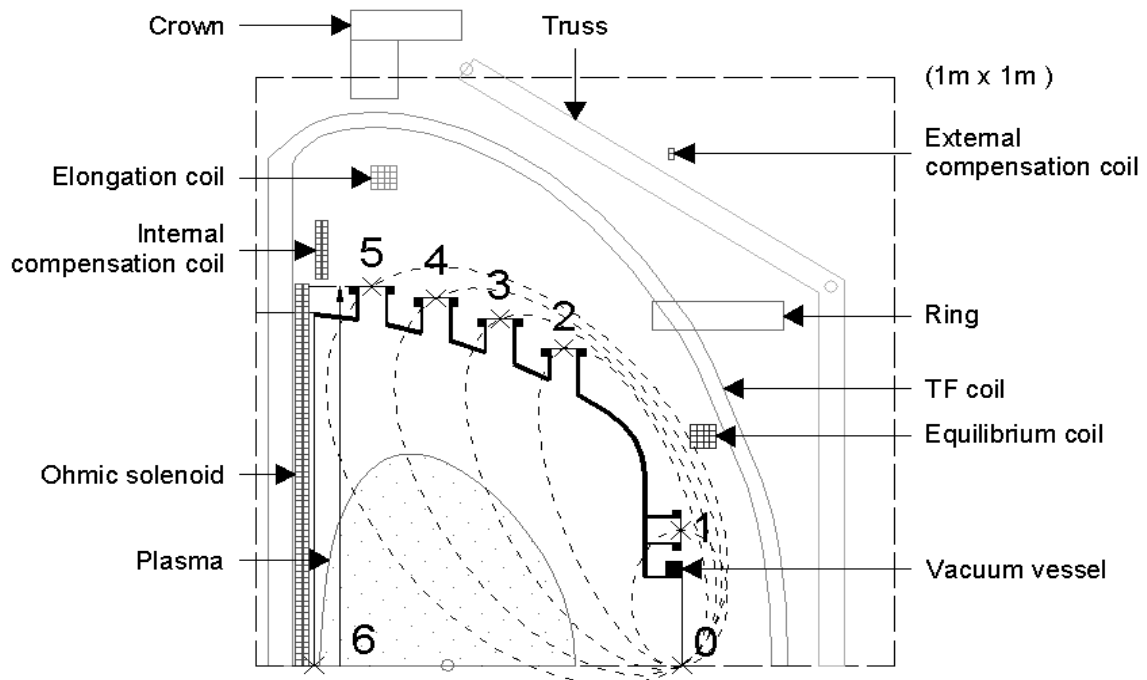


Figure 5: Sections of the vacuum vessel used for measuring the eddy current distribution. The dashed lines indicate schematically the removable Rogowski coil used in the measurements.

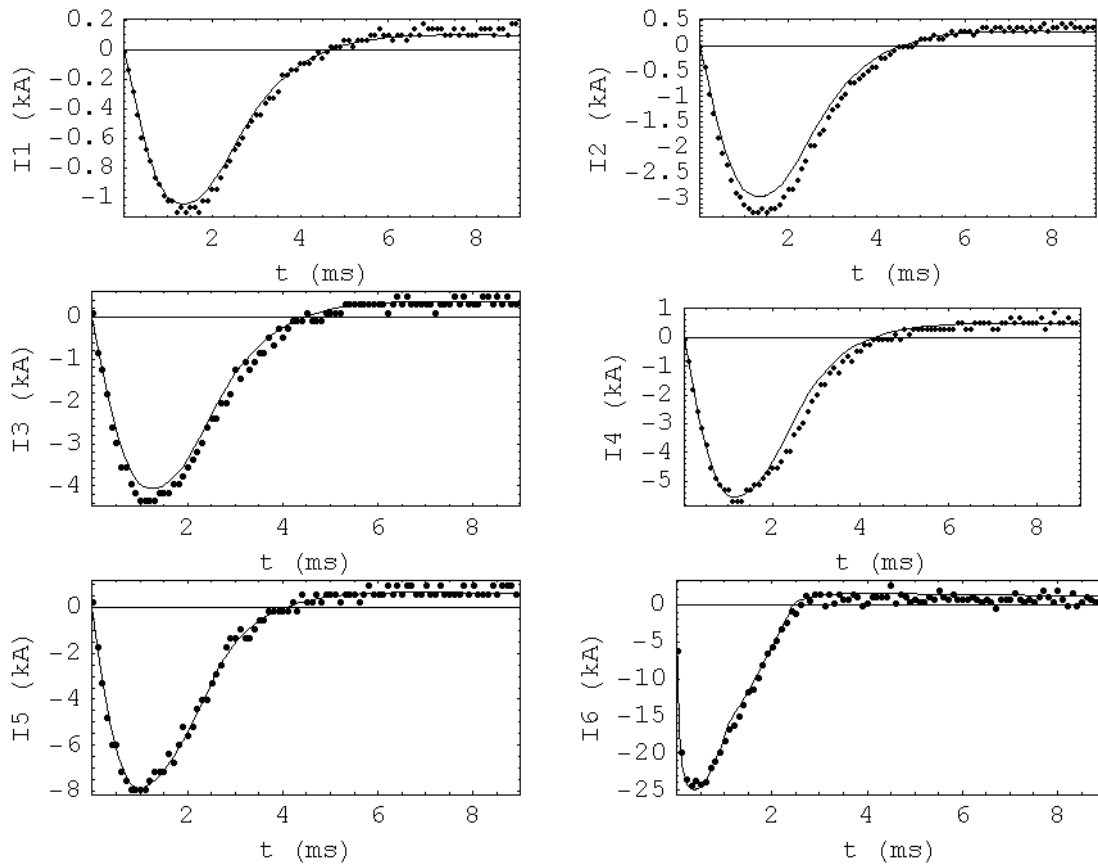


Figure 6: Distribution of eddy currents in sections of the ETE vacuum vessel wall. The continuous line and the disks correspond to calculated and experimental values, respectively.